Journal of Cancer Research and Clinical Oncology (2019) 145:2199–2209
https://doi.org/10.1007/s00432-019-02969-1

ORIGINAL ARTICLE – CANCER RESEARCH

Selective radiofrequency ablation of tumor by magnetically targeting of multifunctional iron oxide–gold nanohybrid

Jaber Beyk[1] · **Hassan Tavakoli**[1,2]

Received: 25 March 2019 / Accepted: 1 July 2019 / Published online: 15 July 2019
© Springer-Verlag GmbH Germany, part of Springer Nature 2019

Abstract

Purpose Radiofrequency (RF) ablation therapy is of great interest in cancer therapy as it is non-ionizing radiation and can effectively penetrate into the tissue. However, the current RF ablation technique is invasive that requires RF probe insertion into the tissue and generates a non-specific heating. Recently, RF-responsive nanomaterials such as gold nanoparticles (AuNPs) and iron oxide nanoparticles (IONPs) have led to tremendous progress in this area. They have been found to be able to absorb the RF field and induce a localized heating within the target, thereby affording a non-invasive and tumor-specific RF ablation strategy. In the present study, for the first time, we used a hybrid core-shell nanostructure comprising IONPs as the core and AuNPs as the shell (IO@Au) for targeted RF ablation therapy. Due to the magnetic core, the nanohybrid can be directed toward the tumor through a magnet. Moreover, IONPs enable the nanohybrid to be used as a magnetic resonance imaging (MRI) contrast agent.

Results In vitro cytotoxicity experiment showed that the combination of IO@Au and 13.56-MHz RF field significantly reduced the viability of cancer cells. Next, during an in vivo experiment, we demonstrated that magnetically targeting of IO@Au to the tumor and subsequent RF exposure dramatically suppressed the tumor growth.

Conclusion Therefore, the integration of targeting, imaging, and therapeutic performances into IO@Au nanohybrid could afford the promise to improve the effectiveness of RF ablation therapy.

Keywords Radiofrequency ablation · Gold nanoparticles · Iron oxide nanoparticles · Magnetic targeting · Magnetic resonance imaging

Introduction

Conventional cancer therapy modalities including surgery, chemotherapy, and radiotherapy have shown limited success in cancer management and often been associated with treatment failure caused by tumor relapse or metastasis. Therefore, intensive efforts have been made in the area of cancer therapy to either improve the effectiveness of the currently available approaches or to develop novel approaches as an alternative. Thermal therapy has attracted a great deal of interest in recent oncology studies. Thermal therapy can be applied in a mild temperature range as an adjuvant therapy to make tumor cells more susceptible to chemotherapy and radiotherapy. It can also be used in thermal ablation range (> 47 °C) as a singular therapy to directly eradicate tumor cells (Wust et al. 2002; van der Zee 2002; Beik et al. 2019).

Radiofrequency (RF) ablation is a common clinical thermal therapy method that utilizes RF waves with a frequency range of 10 kHz–900 MHz (MUDr and Meltem Onder 2014). The effective penetration depth and non-ionizing property of RF waves are the two important advantages that make RF ablation method superior to other modalities such as laser-based treatments and radiotherapy. However, the need for RF probe insertion into the tumor tissue in RF ablation procedures, non-specific tumor heating, and generating unwanted thermal damages in surrounding healthy tissues have considerably restricted the extensive use of RF ablation therapy (Raoof et al. 2013; Raoof and Curley 2011). Recently, nanotechnology has exhibited great promise to expand the clinical utility of RF ablation therapy through introducing potential RF-responsive nanomaterials that offer

✉ Hassan Tavakoli
tavakoli@bmsu.ac.ir

[1] Neuroscience Research Center, Baqiyatallah University of Medical Sciences, Tehran, Iran

[2] Department of Physiology and Biophysics, Baqiyatallah University of Medical Sciences, Tehran, Iran

the ability to generate heat upon RF exposure (Letfullin et al. 2015; Corr and Curley 2017). Therefore, a selective and remote (non-invasive) tumor heating strategy could potentially be realized by targeting RF-responsive nanomaterials to the tumor and subsequent RF exposure using an external source.

Metallic nanoparticles such as gold (AuNPs), iron oxide (IONPs), platinum, cobalt, carbon-based nanomaterials, and silicon nanoparticles have been proposed as potential RF-responsive nanomaterials (Rejinold et al. 2015; Tamarov et al. 2014). Among them, AuNPs and IONPs have been more the subject of recent studies and the mechanism behind the RF heating ability of these nanoparticles is almost well known (Mustafa et al. 2013; Nguyen et al. 2016; Collins et al. 2014; Fang et al. 2019). Accordingly, for the first time in the present study we have employed a hybrid core-shell nanostructure comprising IONPs as the core and AuNPs as the shell (IO@Au) for targeted RF ablation therapy. Beside the RF-responsive feature of this nanohybrid, it can be targeted toward the tumor site by means of an external magnetic field (a magnet) due to its magnetic properties, a method that is called magnetic drug targeting (MDT) (Shapiro et al. 2015). Moreover, the magnetic core enables this nanohybrid to be used as a magnetic resonance imaging (MRI) contrast agent and can, therefore, be detected remotely via MRI (Eyvazzadeh et al. 2017). We evaluated the in vitro RF ablation ability of this nanohybrid against CT26 mouse colon adenocarcinoma cells. Then, during an in vivo experiment, IO@Au was injected into the colon tumor-bearing mice and targeted to the tumor site via a magnet, while the tumor localization of nanoparticles was identified using MRI. Subsequently, mice were exposed to a 13.56-MHz RF field for tumor-specific thermal ablation therapy.

Materials and methods

Materials

Iron (II) chloride tetrahydrate (> 99%), iron (III) chloride hexahydrate (> 99%), ammonia (32%), hydrochloric acid (HCl), nitric acid (HNO_3), *N*-hydroxysuccinimide, and dicyclohexylcarbodiimide were purchased from Merck (Darmstadt, Germany) for synthesis of nanoparticles. Dubelco's Modification of Eagle's Medium (DMEM), fetal bovine serum (FBS), Trypsin-ethylenediaminetetraacetic acid (EDTA), and penicillin–streptomycin were purchased from Sigma-Aldrich Corp. (St Louis, MO, USA) for cell culture experiment.

Preparation and characterization of IO@Au nanohybrid

The synthesis method of IO@Au has been recently described in another reports (Mirrahimi et al. 2017). The concentrations of Au and Fe were measured by inductively coupled plasma mass spectrometry (ICP-MS) analysis of the nanoparticle solution. To determine the size and morphology of the nanohybrid, transmission electron microscopy (TEM; LEO906-ZEISS; Germany) was conducted at 100 kV. In addition, the hydrodynamic size distribution and zeta potential of the nanoparticles in water was investigated by dynamic light scattering (DLS, Zetasizer Nano ZS-90 instrument). X-ray diffraction (XRD) analysis of IO@Au was performed using an X'Pert Pro MPD instrument (PANalytical) with KαCu (1.54 Å) radiation.

Cell culture

CT26 cell line originated from mouse colon adenocarcinoma was obtained from Pasteur Institute of Iran. Cells were cultured in RPMI 1640 medium with 10% FBS, 100 units/ml penicillin, and 100-µg/ml streptomycin at 37 °C in 5% CO_2. To harvest cells for subsequent experiments, cells were trypsinized with 1 mM EDTA/0.25% Trypsin (w/v) in PBS.

In vitro RF ablation therapy

To determine the RF ablation effect of IO@Au, the viability of CT26 cells treated with the combination of IO@Au and RF field was investigated. For this purpose, 1×10^4 CT26 cells were seeded on a 96-well plate and kept in an incubator at 37 °C overnight. Cells were treated with IO@Au at varying concentrations (0–75 µg/ml) for 4 h. Cells were washed three times with PBS to remove the unloaded nanoparticles. Cells were then trypsinized, centrifuged, and resuspended with warm PBS at 37 °C and placed in 1.5-ml Eppendorf tubes. Next, Eppendorf tubes containing cell suspensions were introduced at the center of a water-cooled solenoid RF coil of 8 cm in diameter coupled to a 13.56 MHz RF field generator. Then, cells were subjected to RF field at the power of 100 W for 30 min. The temperature of cell suspensions was continuously measured using an infrared thermal imaging camera (Testo 875-1i, Germany). After RF exposure, cells were seeded again on a 96-well plate and kept in an incubator at 37 °C. After 24 h, the viability of CT26 cells was measured using MTT assay as suggested by the manufacturer's manual (Sigma-Aldrich).

Tumor induction

Male BALB/c mice (5–8 weeks old and weighing 20–25 g) were obtained from Pasteur Institute of Iran. Mice were housed

under controlled light, temperature, and humidity conditions for 1 week before experiments. For tumor induction, after three passages, 2×10^6 CT26 cells suspended in 0.2-ml medium solution were injected subcutaneously on the right flank of mice. The experiments were initiated when the tumor volume grew to approximately 100 mm^3. All animal experiments were conducted in accordance with the guidelines established by the Institutional Animal Care Committee.

MRI study

Due to the presence of IONPs in the core of the synthesized IO@Au, this nanohybrid is expected to enhance the T2 MR signal intensity. First, the capacity of IO@Au to shorten the T2 relaxation rate of water protons was evaluated by relaxivity measurement. The solutions of IO@Au at varying Fe concentrations of 0.03, 0.06, 0.12, 0.25, 0.5, and 1 mM were prepared and underwent MRI. T2 relaxivity was determined using the following acquisition parameters: spin-echo, TR 3000 ms, TE 12–384 ms, slice thickness 3 mm, and FOV of 256 mm × 128 mm. Furthermore, MRI study was performed to identify the tumor localization of IO@Au nanohybrid. For this purpose, three animal groups were considered including: control (without injection), intravenous (I.V) injection of IO@Au and I.V injection of IO@Au followed by magnetic targeting (MDT). For I.V injection alone, mice were injected with 0.2 ml of IO@Au solution ([Fe]: 2 mM) through the tail vein and imaged 24 h post-injection. For MDT group, after I.V injection (with the same concentration), a magnet (magnetic field strength of 0.4 Tesla) was placed on the tumor to accumulate nanoparticles within the tumor, and then, the mice were imaged. MRI examination was executed using Philips superconductor clinical MR system (1.5 T) with the following acquisition parameters: T2* weighted gradient echo, TR 250 ms, TE 11 ms, FA 25, slice thickness 2 mm, and FOV of 386 mm × 248 mm.

In vivo RF ablation therapy

Next, the RF-responsive potential of IO@Au was utilized for thermal ablation of CT26 tumor. CT26 tumor-bearing mice were randomly divided into four groups ($n=5$) including: control (untreated), RF exposure (13.56 MHz, 100 W, 20 min), I.V injection of IO@Au ([Au]: 4 mM, [Fe]: 2 mM, 0.2 ml) + RF exposure, and I.V injection of IO@Au + MDT + RF exposure. For non-targeted group, RF exposure was performed 24 h post-injection. For MDT group, a magnet was placed on the tumor immediately after injection for 3 h, and thereafter, mice were exposed to the RF field. For RF exposure, the whole body of mouse was placed inside the RF coil and only the tail was kept outside to avoid overheating. During the RF operation, the temperature of the tumor was monitored in real time using a thermal imaging camera. The tumor volume change was monitored during 21 days of study period and the tumor growth profile was plotted versus time. The tumor volume was calculated as: $\frac{\pi}{6}\times \text{length}\times(\text{width})^2$. Histological examination of tumor tissue extracted from mice was performed at 48 h post-treatment using hematoxylin–eosin (H&E) staining. Moreover, immunohistochemistry was performed at 48 h post-treatment using a TUNEL staining kit (Roche) according to the manufacturer's instructions to identify the extent of apoptosis in tumor tissue.

Real-time quantitative PCR (RT-qPCR)

We carried out RT-qPCR to determine the changes in the mRNA expression level of pro-apoptotic Bax and anti-apoptotic Bcl-2 factors. First, tumor-bearing mice were subjected to various treatments as described above and then scarified at 48-h post-treatment and the tumors were harvested. The total RNA extraction from the tumors was carried out using *AccuZol* as per the manufacturer's instructions (BioNeer Corporation, South Korea). One microgram of the total RNA was reverse transcribed into cDNA using RevertAid First Strand cDNA Synthesis Kit (Thermo Scientific, Carlsbad, CA, USA). Then, RT-qPCR was performed on a Corbett 65H0 machine (Corbett Research, Sidney, Australia) using SYBR® Premix Ex Taq II (Takara, Otsu, Japan). Table 1 represents the primer sequences of Bax and Bcl-2 as the apoptosis-related genes and β-actin gene as the internal control.

Statistical methods

Statistical analysis was performed by one-way ANOVA test using SPSS software (version11). Then, the Tukey's test at 95% confidence level was used as a post hoc test for pairwise comparison of means of the treatment groups. Measurement data are mean ± standard deviation (SD). A value of $P<0.05$ was considered statistically significant.

Table 1 Sequences of primer sets used for RT-qPCR analysis

Primer name	Forward oligo sequences	Reverse oligo sequences
Bax	GAGCTGCAGAGGATGATTGC	CTTGGATCCAGACAAGCAGC
Bcl-2	TCAGCATTGCGGAGGAAGTA	CCTTCCCCGAAAAGAAGCTG
β-Actin	TTGAGACCTTCAACACCCCA	TGATGTCACGCACGATTTCC

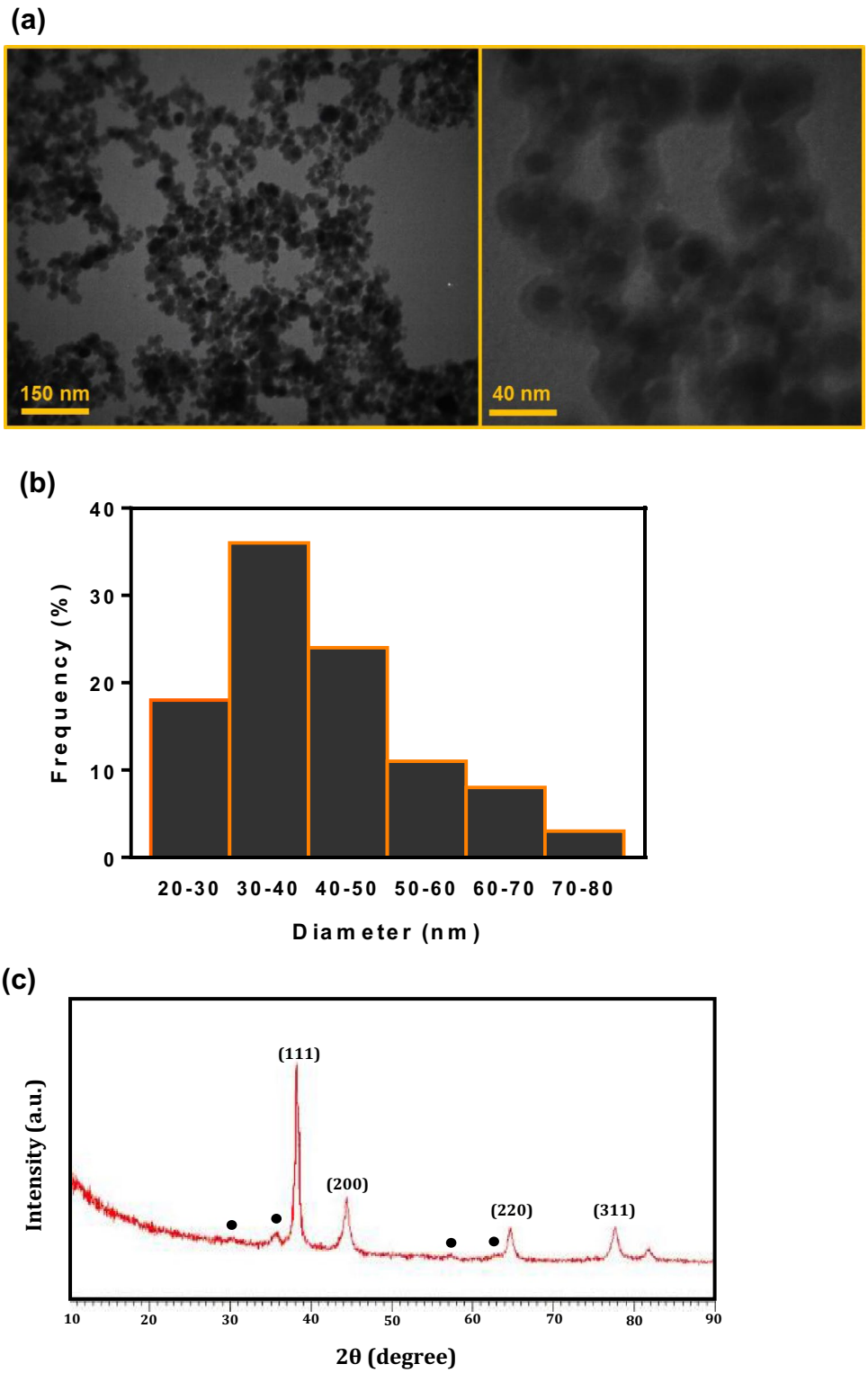

Fig. 1 Characterization of IO@Au nanohybrid. **a** TEM image in two magnifications indicates the well-defined core-shell structure of IO@Au. **b** Hydrodynamic size distribution histogram, showing the maximum frequency of ~ 37 nm. **c** XRD pattern of IO@Au. The diffraction peaks are attributed to Au, and the black circles indicate the characteristic peak positions of IONPs which no longer appear in IO@Au

Results

Characterization of IO@Au

As shown in Fig. 1a, TEM analysis of IO@Au confirmed the well-defined core-shell structure of this nanohybrid wherein IONPs of ~ 23 nm in diameter as the core are clearly covered by ~ 5-nm-thick Au shells. DLS measurement (Fig. 1b) was shown that IO@Au has a hydrodynamic size ranging from 20 to 80 nm with the maximum frequency around ~ 37 nm. The zeta potential of IO@Au was also found to be − 27.2 mV, ensuring the stability of particles in colloidal dispersion. The

crystalline structure of the synthesized IO@Au characterized by XRD also proved that Au shell has been formed on IONPs (Fig. 1c). The characteristic peaks of IONPs at 30.57°, 35.54°, 57.14°, and 62.78° are disappeared after Au coating, as indicated by black circles. The diffraction peak positions of IO@Au at 38.18°, 44.35°, 64.60°, and 77.57° can be related to (111), (200), (220), and (311) planes of Au, respectively. This indicates the formation of IO@Au core-shell nanohybrid structure.

In vitro cytotoxicity experiment

To determine the cytotoxicity of RF irradiation alone, CT26 cells were exposed to a 13.56 MHz RF field at a fixed power of 100 W for varying exposure durations from 2 to 30 min. As shown in Fig. 2a, RF alone did not induce notable cytotoxicity in CT26 cells and only less than 10% cell death was observed even for cells subjected to the longest RF exposure time (30 min). Next, the cytotoxicity of IO@Au was tested in CT26 cells treated with varying concentrations of nanoparticles. Figure 2b shows that IO@Au has an acceptable biocompatibility where IO@Au at the highest tested concentration of 75 µg/ml led to 16% cell death. In contrast, the combination of IO@Au + RF significantly reduced the cell viability, demonstrating the RF-responsive ability of IO@Au. While the separate application of RF (30 min) and IO@Au (75 µg/ml) caused 8.5% and 16% cell death, respectively, the combination of IO@Au + RF acted synergistically and induced a markedly higher cell death rate of 84%. The temperature of cell suspensions was also recorded during RF irradiation. For cells treated with IO@Au (75 µg/ml), the temperature was increased by 5.1 °C after 8 min RF irradiation and remained constant up to 30 min, whereas cells without nanoparticles showed a temperature rise of 2.8 °C after 5 min RF irradiation and then reached to steady-state temperature.

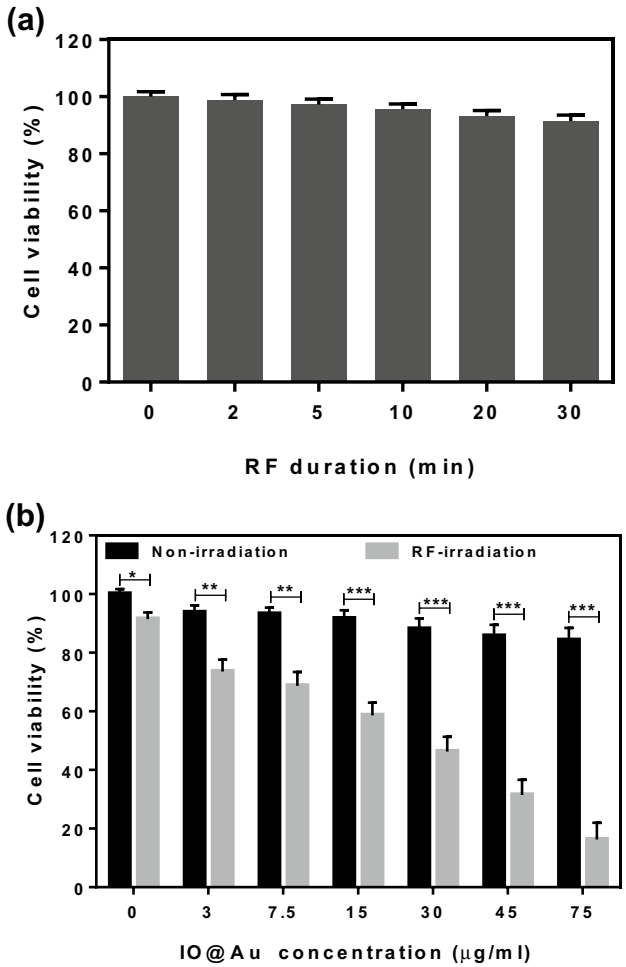

Fig. 2 In vitro cytotoxicity experiment. **a** The viability of CT26 cells subjected to varying RF exposure durations (13.56 MHz, 100 W). **b** The viability of CT26 cells treated with various concentrations of IO@Au (4 h) followed by 13.56 RF field exposure (100 W, 30 min). (*P value < 0.05, **P value < 0.01, and ***P value < 0.001)

MRI study

T2-weighted MR images of IO@Au solution revealed that a gradual decrease in the MR signal intensity can be observed with the increase of Fe concentration. By linear fitting the T2 relaxation rate (1/T2) versus Fe concentration, the transverse relaxivity ($r2$) of IO@Au was calculated to be 98/Mm/S (Fig. 3a). Then, the ability of IO@Au to create a negative contrast in T2-weighted MR images was utilized to detect its in vivo localization. First, the MR image of mice without IO@Au injection was acquired to identify the base level of soft-tissue image contrast (Fig. 3b). MRI study of mice 24 h following I.V injection of IO@Au shows that nanoparticles are trafficked to the tumor and generate hypointense areas (dark spots) in T2-weighted MR image (Fig. 3c). For mice that were subjected to a magnet for tumor targeting of nanoparticles, a clearly visible hypointense area can be detected in the tumor, evidencing the spatial location of nanoparticles (Fig. 3d). The quantitative MR image analysis reveals that the baseline level of tumor signal intensity was 251 ± 5 and significantly decreased to 219 ± 8 and 123 ± 11 after I.V injection and I.V injection + MDT, respectively (Fig. 3e). This result validates the enhanced tumor accumulation of IO@Au under MDT.

IO@Au nanohybrid enhances RF-induced heating

To determine the effect of IO@Au nanohybrid on RF-induced heating, the temperature of tumor with and without IO@Au injection was monitored in real time during RF excitation using a thermal camera. As shown in Fig. 4, RF exposure alone at the power of 100 W increased the tumor temperature to 43 °C after 20 min. In contrast, the mice pretreated with IO@Au exhibited an enhanced temperature rise

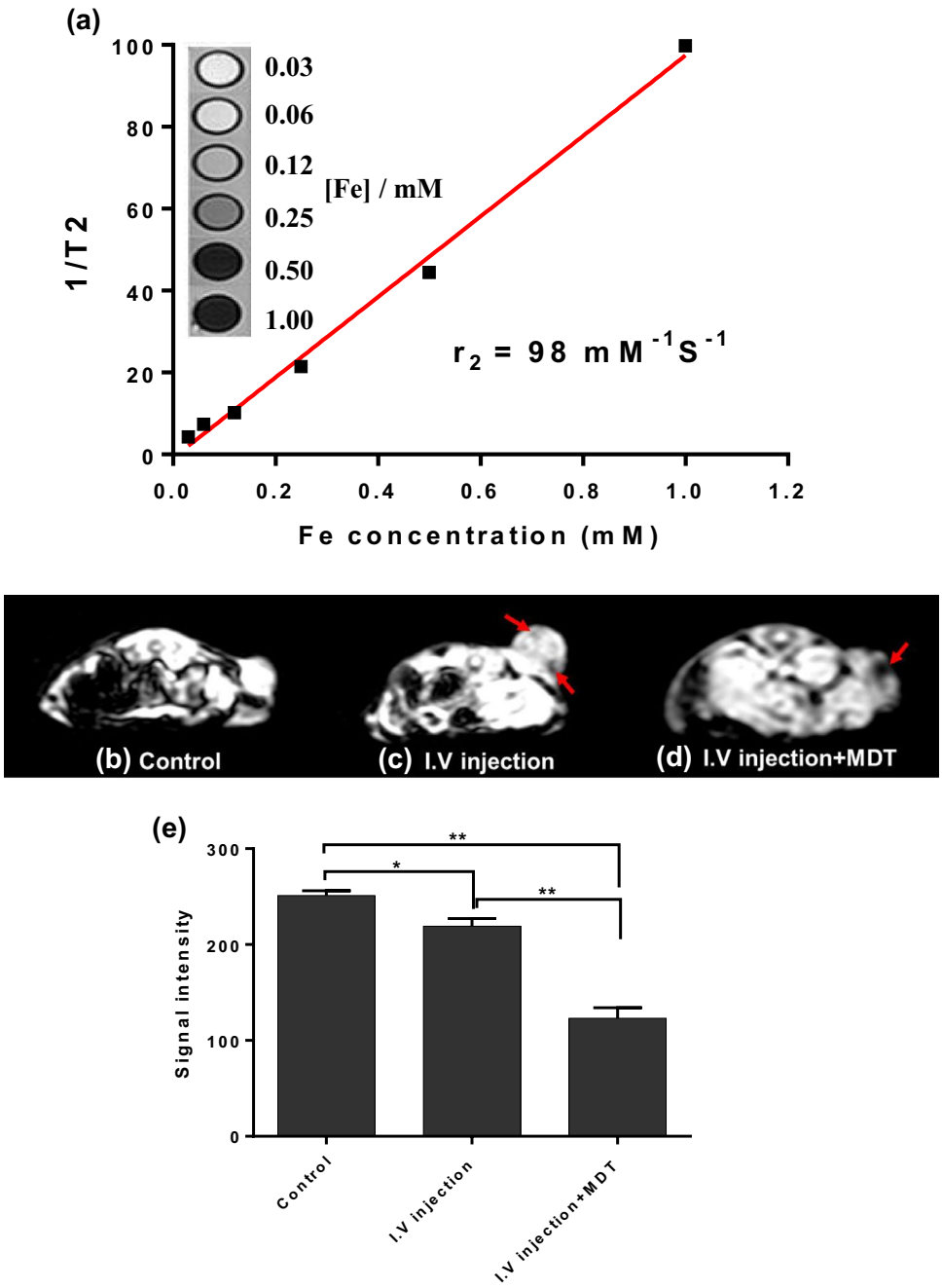

Fig. 3 MRI study. **a** Transverse relaxation rate (1/T2) of IO@Au as a function of Fe concentration (inset: T2-weighted MR images of IO@Au solutions). Representative T2-weighted MR images of CT26 tumor-bearing mice (**b**) without nanoparticle injection, **c** at 24-h post I.V injection of IO@Au, and **d** at 3-h post I.V injection followed by magnetic targeting of IO@Au (arrows indicate the spatial location of IO@Au). **e** MR signal intensity, showing the T2-enhancement capability of IO@Au. (**P* value < 0.05, ***P* value < 0.001)

rate during RF operation. The final temperature of tumor treated with I.V injection and I.V injection + MDT reached to 46 and 49.5 °C, respectively, after 20-min RF exposure. This result supports the heat generation potential of IO@Au upon RF field exposure. Meanwhile, the higher temperature rise rate of tumor in magnetically targeted group than non-targeted group further proves the effective role of magnetic targeting on increasing the intratumoral concentration of IO@Au.

In vivo RF ablation therapy

Next, the RF-responsive potential of IO@Au nanohybrid was tested for thermal ablation of CT26 tumor. Figure 5a shows the tumor volume changes of mice during 21 days of study period. It can be seen from this figure that RF irradiation alone for 20 min inhibited the tumor growth to some extent within several days after the treatment, compared to the untreated mice. However, the rate of tumor growth was increased after several days post-treatment and the tumor volume reached to nearly 40 times larger than that of initial

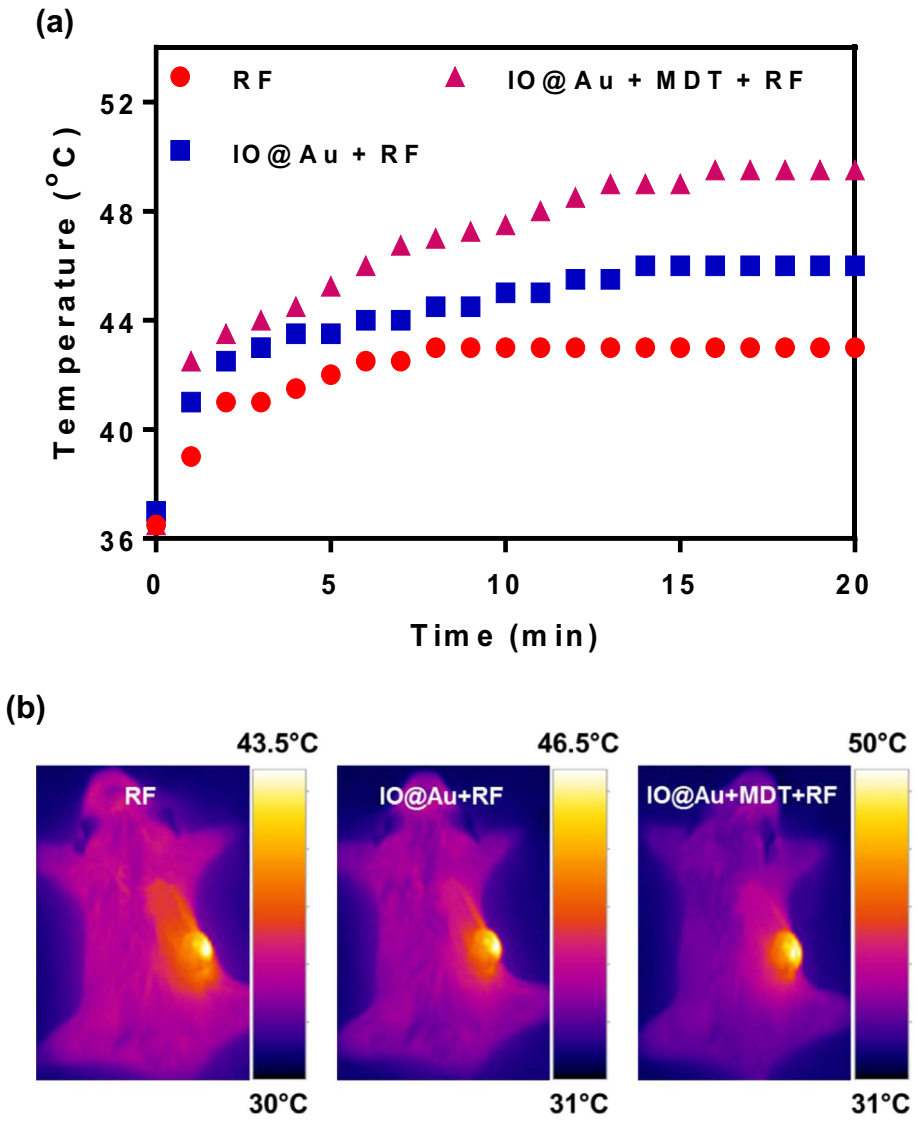

Fig. 4 In vivo tumor thermometry. **a** Temperature rise profile of tumor as a function of RF field exposure (13.56 MHz, 100 W) and **b** representative thermal images of CT26 tumor-bearing mice at the end of RF treatment (after 20 min)

tumor on day 21. The mice treated with I.V injection of IO@Au + RF indicated a significantly smaller tumor volume compared to those mice treated with RF alone. The relative tumor volume of mice in I.V injection + RF group at 21 day post-treatment was approximately 16 times larger than that of initial tumor, demonstrating the tumor inhibition rate of ~ 70%: $\left(\text{tumor inhibition rate} = 1 - \frac{V_{\text{treatment}}}{V_{\text{control}}};\ V \text{ stands for tumor volume}\right)$. Surprisingly, I.V injection of IO@Au followed by magnetic targeting prior to RF operation dramatically shrunk the tumor mass, yielding the tumor inhibition rate of ~ 92%. Representative photographs of the mice on day 21 post-treatment (Fig. 5b) obviously indicate the tumor ablation ability of various treatment regimens, wherein I.V injection + MDT + RF suppressed the tumor growth and left a black scar at the tumor site as the evidence of necrosis. To further demonstrate the antitumor activity of IO@Au in combination with RF irradiation, the histological analysis of tumor tissue was performed using H&E and TUNEL staining methods (Fig. 6). As shown in Fig. 6a, the tumor section of mice treated with RF alone indicates normal cell morphology along with a slight decrease in cell density compared to the control. However, a significant reduction in cell density and extensive area of necrosis can be clearly seen in the tumor section of mice treated with the combination of IO@Au and RF exposure, further confirming the enhancement of RF ablation therapy due to the presence of IO@Au nanohybrid. Moreover, an extensive area of TUNEL-positive cells (apoptotic cells) indicated in brown can be observed in the tumor sections of mice receiving IO@Au followed by RF exposure, whereas no evidence of TUNEL-positive cells was detected in the tumor tissue of mice in control and RF alone groups. Accordingly, it can be concluded that the combination of IO@Au and RF exposure can induce cell death via apoptosis in tumor cells (Fig. 6b).

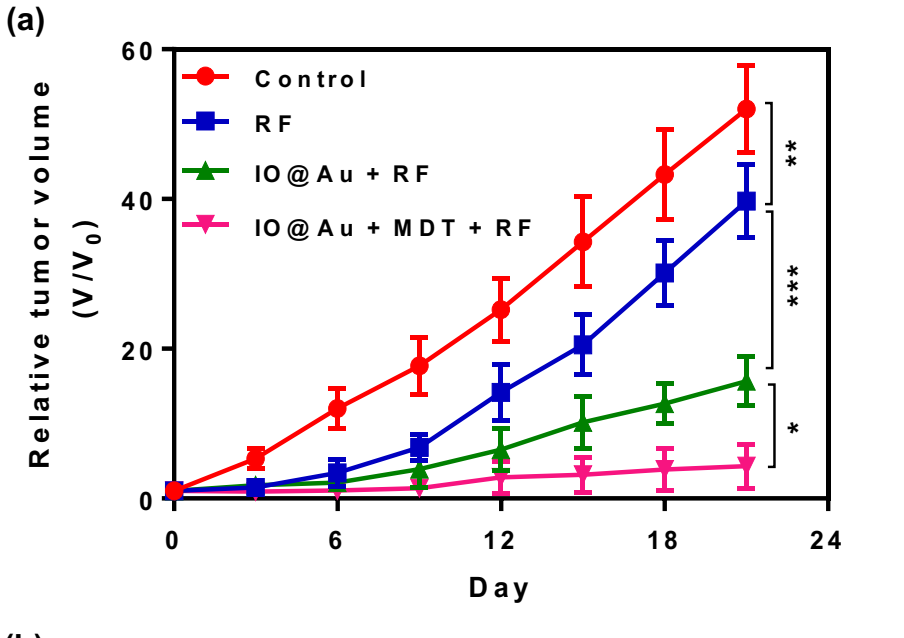

Fig. 5 In vivo antitumor assessment. **a** The tumor volume change profiles as a function of time post-treatment relative to the initial tumor volume at day 0. (*P value < 0.05, **P value < 0.01, and ***P value < 0.001). **b** Representative photographs of CT26 tumor-bearing mice at the end of study period (day 21)

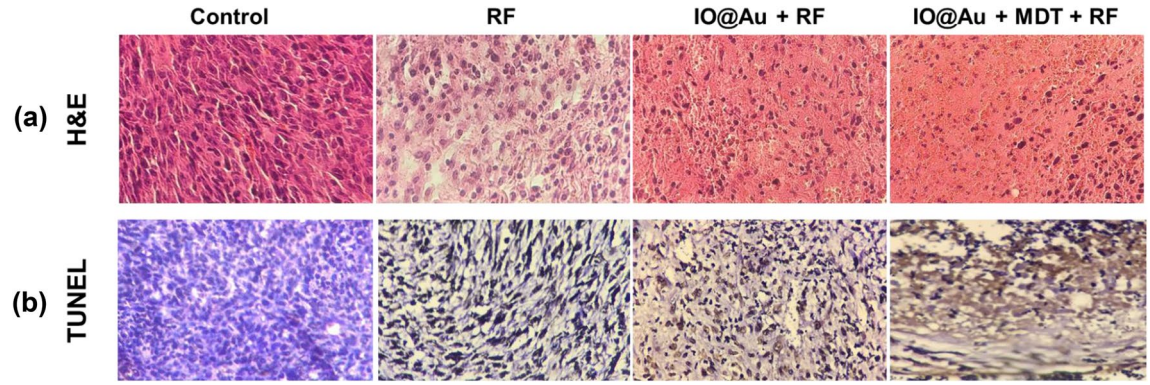

Fig. 6 Histological examination. Representative H&E and TUNEL staining images of CT26 tumor extracted from mice at 48 h post-treatment

Gene expression analysis

To investigate whether the combination of RF and IO@Au can trigger the signaling pathway of apoptosis, the alternations in the mRNA expression level of two apoptosis-related genes were explored by RT-qPCR technique. As shown in Fig. 7, RF exposure alone did not notably alter the expression level of Bcl-2 anti-apoptotic factor, whereas a significant down-regulation of Bcl-2 mRNA level was detected in tumors treated with IO@Au + RF (0.67-fold) and IO@Au + MDT + RF (0.38-fold), compared to control group. In contrast, the expression level of Bax pro-apoptotic factor was significantly up-regulated in tumors treated with IO@Au + RF and IO@Au + MDT + RF by 1.82- and 2.18-fold compared to control group, respectively ($P < 0.001$). Therefore, the elevated expression of Bax together with the depressed expression of Bcl-2 demonstrated that IO@Au in combination with RF exposure could trigger apoptosis in tumor cells.

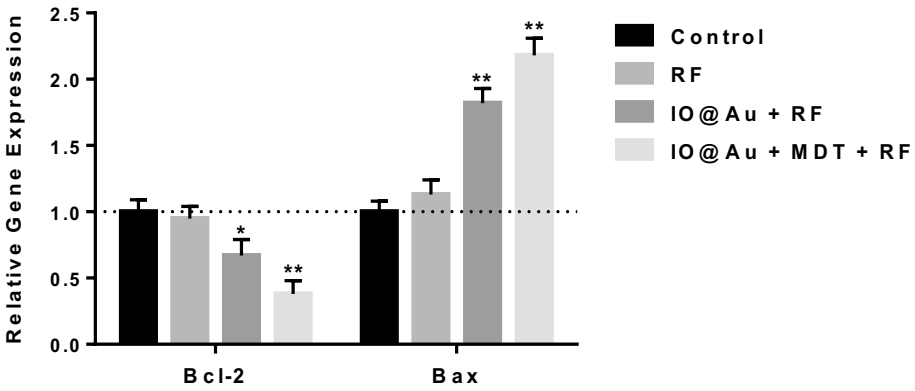

Fig. 7 Gene expression analysis. The mRNA expression level of Bax and Bcl-2 in CT26 tumor after various treatments relative to control (asterisks indicate the statistical difference with control group, **P* value < 0.05, ***P* value < 0.001)

Discussion

To date, several nanotechnology-mediated thermal therapy approaches have been developed wherein thermo-responsive nanoparticles are used to absorb the energy of external hyperthermia source to induce a localized heating into the target (Beik et al. 2016a, b, 2018). Nanoparticle-assisted photothermal therapy is a nanotechnology-mediated thermal therapy approach in which the heat generated due to interaction between plasmonic nanomaterials, e.g., AuNPs and incident laser light is exploited for thermal ablation of tumor (Beik et al. 2017; Mirrahimi et al. 2019; Ghaznavi et al. 2017). However, the limited penetration depth of laser light into the tissue highly hampers the clinical utility of this approach. On the contrary, RF waves can be offered as an ideal hyperthermia source, since they are able to efficiently penetrate into the body and heat up the deep-seated tumors (Zhang et al. 2016a, b). Recently, a number of RF-responsive nanomaterials have been identified which are able to absorb the RF field and generate heat, thereby developing a nanotechnology-mediated RF hyperthermia.

The principle of heat generation through nanoparticles under RF field heavily relies on the type of RF antenna. Typically, two designs of the RF antenna are used to induce hyperthermia, including inductively coupled device that produces an alternating magnetic field (AMF) inside a solenoid and capacitively coupled device that produces an alternating electric field between parallel-plates (Pantano et al. 2017). It has been demonstrated that magnetic nanoparticles can be stimulated upon AMF and generate heat which establishes the concept of magnetic hyperthermia. Two main mechanisms are known to contribute in heat generation via magnetic nanoparticles upon AMF excitation, including magnetic friction (Néel relaxation) and viscous friction (Brownian relaxation). Néel relaxation is the result of random flips of the magnetic moments (spins) and dominates in particles less than 10–20 nm in diameter, whereas Brownian relaxation originates from free rotation of the entire particle and becomes dominant in larger particles (Hergt et al. 2006; Rosensweig 2002). In this study, we used an inductively coupled RF device, and therefore, the enhanced heating rate of tumor treated with IO@Au can be mainly attributed to the magnetic core of this nanohybrid that generates heat upon AMF excitation.

Many studies have also investigated the RF-responsive properties of AuNPs to achieve a non-invasive RF hyperthermia (Corr and Curley 2017; Glazer et al. 2010). Although these studies have demonstrated an enhanced heating rate and antitumor response in the presence of AuNPs, the principle mechanism by which AuNPs generate heat as exposed to RF field has been the subject of controversy. Several mechanisms have been proposed to explain how non-magnetic metallic nanoparticles can generate heat under an RF field. First, Curley et al. proposed a Joule heating model in which AuNPs were assumed as conductors and the RF-mediated heating was related to resistive dissipation of RF electric field within AuNPs (Moran et al. 2009). Today, it has been both theoretically and experimentally found that AuNPs themselves could not generate heat and the temperature rise of AuNPs suspensions is due to background electrolyte resistive heating (Letfullin et al. 2015; Liu et al. 2012; Li et al. 2011; Sassaroli et al. 2012; Pearce and Cook 2011; Tamarov et al. 2017). Two new mechanisms, magnetic heating and electrophoretic heating, have been introduced to be attributed to the RF-mediated heating of AuNPs. Magnetic heating is based on the fact that AuNPs can become magnetic after chemical oxidation and, therefore, generate heat under AMF generated by an inductively coupled RF device through Néel and Brownian relaxations. However, this mechanism does not appear to be the case here, since superatomic paramagnetism has only been observed for Au nanoclusters smaller than 2.5 nm in diameter (Pearce and Cook 2011; Nealon et al. 2012). Electrophoretic heating refers to the movement of charged particles on the AuNPs surface in response to a time-varying electric field that leads to oscillation of AuNPs, thus generating heat through frictional mechanisms (Sassaroli et al. 2012; Corr et al.

2012; Collins et al. 2018). Given that a non-uniform time-varying electric field can be generated in an RF solenoid coil (Lee et al. 2005), the electrophoretic mechanism may involve in the heating of the AuNPs on IONPs (Park et al. 2018). Taken together, the observed heating here can be mainly attributed to the magnetic moment of IONPs and partially to the electrophoretic motion of AuNPs.

In the resent study, we utilized a core-shell nanostructure of IONPs and AuNPs for targeted RF ablation therapy. The magnetic core of this nanohybrid allows to target it toward the tumor using an external magnetic field and also determine its in vivo biodistribution through MRI. The MR images of mice revealed that IO@Au can be effectively localized in the tumor through magnetic targeting. Next, the in vivo tumor thermometry experiment demonstrated that the magnetically targeting of IO@Au followed by RF exposure can effectively heat up the tumor. Consequently, the antitumor studies manifested that IO@Au in combination with RF exposure can remarkably suppress the tumor growth, supporting the potent antitumor efficacy of this strategy.

Conclusion

To summarize, we presented a multifunctional RF-responsive IO@Au core-shell nanohybrid that can be used for targeted RF ablation therapy. The magnetic core allows the nanohybrid to be magnetically targeted to the tumor and remotely tracked via MRI. The existence of IO@Au noticeably enhanced RF-induced heating and induced a potent antitumor response, resulting in effective tumor shrinkage. The results of this study support that IO@Au is able to expand the RF ablation therapy through bypassing the invasive procedure of RF probe insertion and focusing the RF-induced damages to the tumor while avoiding the surrounding normal tissues from unwanted heating.

Funding This study was funded by Baqiyatallah University of Medical Sciences.

Compliance with ethical standards

Conflict of interest The authors declare that they have no conflict of interest.

Ethical approval All applicable international, national, and/or institutional guidelines for the care and use of animals were followed.

References

Beik J, Abed Z, Ghoreishi FS, Hosseini-Nami S, Mehrzadi S, Shakeri-Zadeh A, Kamrava SK (2016a) Nanotechnology in hyperthermia cancer therapy: from fundamental principles to advanced applications. J Control Release 235:205–221

Beik J, Abed Z, Ghadimi-Daresajini A, Nourbakhsh M, Shakeri-Zadeh A, Ghasemi MS, Shiran MB (2016b) Measurements of nanoparticle-enhanced heating from 1 MHz ultrasound in solution and in mice bearing CT26 colon tumors. J Therm Biol 62:84–89

Beik J, Khademi S, Attaran N, Sarkar S, Shakeri-Zadeh A, Ghaznavi H, Ghadiri H (2017) A nanotechnology-based strategy to increase the efficiency of cancer diagnosis and therapy: folate-conjugated gold nanoparticles. Curr Med Chem 24:4399–4416

Beik J, Shiran MB, Abed Z, Shiri I, Ghadimi-Daresajini A, Farkhondeh F, Ghaznavi H, Shakeri-Zadeh A (2018) Gold nanoparticle-induced sonosensitization enhances the antitumor activity of ultrasound in colon tumor-bearing mice. Med Phys 45:4306–4314

Beik J, Khateri M, Khosravi Z, Kamrava SK, Kooranifar S, Ghaznavi H, Shakeri-Zadeh A (2019) Gold nanoparticles in combinatorial cancer therapy strategies. Coord Chem Rev 387:299–324

Collins C, McCoy R, Ackerson B, Collins G, Ackerson C (2014) Radiofrequency heating pathways for gold nanoparticles. Nanoscale 6:8459–8472

Collins CB, Tofanelli MA, Noblitt SD, Ackerson CJ (2018) Electrophoretic mechanism of Au25 (SR) 18 heating in radiofrequency fields. J Phys Chem Lett 9:1516–1521

Corr S, Curley S (2017) Gold nanoparticles for noninvasive radiofrequency cancer hyperthermia. In: Nanotechnology in cancer. Elsevier, pp 1–18. https://doi.org/10.1016/B978-0-323-39080-4.00001-X

Corr SJ, Raoof M, Mackeyev Y, Phounsavath S, Cheney MA, Cisneros BT, Shur M, Gozin M, McNally PJ, Wilson LJ (2012) Citrate-capped gold nanoparticle electrophoretic heat production in response to a time-varying radio-frequency electric field. J Phys Chem C 116:24380–24389

Eyvazzadeh N, Shakeri-Zadeh A, Fekrazad R, Amini E, Ghaznavi H, Kamrava SK (2017) Gold-coated magnetic nanoparticle as a nanotheranostic agent for magnetic resonance imaging and photothermal therapy of cancer. Lasers Med Sci 32:1469–1477

Fang Y, Li H-Y, Yin H-H, Xu S-H, Ren W-W, Ding S-S, Tang W-Z, Xiang L-H, Wu R, Guan X (2019) Radiofrequency-sensitive longitudinal relaxation tuning strategy enabling the visualization of radiofrequency ablation intensified by magnetic composite. ACS Appl Mater Interfaces 11:11251–11261

Ghaznavi H, Hosseini-Nami S, Kamrava SK, Irajirad R, Maleki S, Shakeri-Zadeh A (2017) Folic acid conjugated PEG coated gold–iron oxide core-shell nanocomplex as a potential agent for targeted photothermal therapy of cancer. Artif Cells Nanomed Biotechnol 46(8):1594–1604

Glazer ES, Zhu C, Massey KL, Thompson CS, Kaluarachchi WD, Hamir AN, Curley SA (2010) Noninvasive radiofrequency field destruction of pancreatic adenocarcinoma xenografts treated with targeted gold nanoparticles. Clin Cancer Res Off J Am Assoc Cancer Res 16:5712–5721

Hergt R, Dutz S, Müller R, Zeisberger M (2006) Magnetic particle hyperthermia: nanoparticle magnetism and materials development for cancer therapy. J Phys Condens Matter 18:S2919

Lee S, Lee Y, Yu I (2005) Electric field in solenoids. Jpn J Appl Phys 44:5244

Letfullin RR, Letfullin AR, George TF (2015) Absorption efficiency and heating kinetics of nanoparticles in the RF range for selective nanotherapy of cancer. Nanomed Nanotechnol Biol Med 11:413–420

Li D, Jung YS, Tan S, Kim HK, Chory E, Geller DA (2011) Negligible absorption of radiofrequency radiation by colloidal gold nanoparticles. J Colloid Interface Sci 358:47–53

Liu X, Chen H-J, Chen X, Parini C, Wen D (2012) Low frequency heating of gold nanoparticle dispersions for non-invasive thermal therapies. Nanoscale 4:3945–3953

Mirrahimi M, Hosseini V, Kamrava SK, Attaran N, Beik J, Kooranifar S, Ghaznavi H, Shakeri-Zadeh A (2017) Selective heat generation in cancer cells using a combination of 808 nm laser irradiation and the folate-conjugated Fe2O3@ Au nanocomplex. Artif Cells Nanomed Biotechnol 46(sup1):241–253

Mirrahimi M, Abed Z, Beik J, Shiri I, Dezfuli AS, Mahabadi VP, Kamrava SK, Ghaznavi H, Shakeri-Zadeh A (2019) A thermo-responsive alginate nanogel platform co-loaded with gold nanoparticles and cisplatin for combined cancer chemo-photothermal therapy. Pharmacol Res 143:178–185

Moran C, Wainerdi S, Cherukuri T, Kittrell C, Wiley B, Nicholas N, Curley S, Kanzius J, Cherukuri P (2009) Size-dependent joule heating of gold nanoparticles using capacitively coupled radiofrequency fields. Nano Res 2:400–405

MUDr KF, Meltem Onder M (2014) Selective radiofrequency therapy as a non-invasive approach for contactless body contouring and circumferential reduction. J Drugs Dermatol 13:291–296

Mustafa T, Zhang Y, Watanabe F, Karmakar A, Asar MP, Little R, Hudson MK, Xu Y, Biris AS (2013) Iron oxide nanoparticle-based radio-frequency thermotherapy for human breast adenocarcinoma cancer cells. Biomater Sci 1:870–880

Nealon GL, Donnio B, Greget R, Kappler J-P, Terazzi E, Gallani J-L (2012) Magnetism in gold nanoparticles. Nanoscale 4:5244–5258

Nguyen DT, Tzou WS, Zheng L, Barham W, Schuller JL, Shillinglaw B, Quaife RA, Sauer WH (2016) Enhanced radiofrequency ablation with magnetically directed metallic nanoparticles. Circ Arrhythm Electrophysiol 9:e003820

Pantano P, Harrison CD, Poulose J, Urrabazo D Jr, Norman TQ, Braun EI, Draper RK, Overzet LJ (2017) Factors affecting the 13.56-MHz radio-frequency-mediated heating of gold nanoparticles. Appl Spectrosc Rev 52:821–836

Park S-I, Chung S-H, Kim H-C, Lee SG, Lee SJ, Kim H, Kim H, Jeong SW (2018) Prolonged heating of Fe3O4–Au hybrid nanoparticles in a radiofrequency solenoid coil. Colloids Surf A 538:304–309

Pearce JA, Cook JR (2011) Heating mechanisms in gold nanoparticles at radio frequencies. In: 2011 Annual International Conference of the IEEE Engineering in Medicine and Biology Society, IEEE, pp 5577–5580

Raoof M, Curley SA (2011) Non-invasive radiofrequency-induced targeted hyperthermia for the treatment of hepatocellular carcinoma. Int J Hepatol 2011:676957

Raoof M, Cisneros BT, Corr SJ, Palalon F, Curley SA, Koshkina NV (2013) Tumor selective hyperthermia induced by short-wave capacitively-coupled RF electric-fields. PLoS One 8:e68506

Rejinold NS, Jayakumar R, Kim Y-C (2015) Radio frequency responsive nano-biomaterials for cancer therapy. J Control Release 204:85–97

Rosensweig RE (2002) Heating magnetic fluid with alternating magnetic field. J Magn Magn Mater 252:370–374

Sassaroli E, Li K, O'Neill B (2012) Radio frequency absorption in gold nanoparticle suspensions: a phenomenological study. J Phys D Appl Phys 45:075303

Shapiro B, Kulkarni S, Nacev A, Muro S, Stepanov PY, Weinberg IN (2015) Open challenges in magnetic drug targeting. Wiley Interdiscip Rev Nanomed Nanobiotechnol 7:446–457

Tamarov KP, Osminkina LA, Zinovyev SV, Maximova KA, Kargina JV, Gongalsky MB, Ryabchikov Y, Al-Kattan A, Sviridov AP, Sentis M (2014) Radio frequency radiation-induced hyperthermia using Si nanoparticle-based sensitizers for mild cancer therapy. Sci Rep 4:7034

Tamarov K, Gongalsky M, Osminkina L, Huang Y, Omar M, Yakunin V, Ntziachristos V, Razansky D, Timoshenko V (2017) Electrolytic conductivity-related radiofrequency heating of aqueous suspensions of nanoparticles for biomedicine. Phys Chem Chem Phys 19:11510–11517

van der Zee J (2002) Heating the patient: a promising approach? Ann Oncol 13:1173–1184

Wust P, Hildebrandt B, Sreenivasa G, Rau B, Gellermann J, Riess H, Felix R, Schlag P (2002) Hyperthermia in combined treatment of cancer. Lancet Oncol 3:487–497

Zhang K, Li P, Chen H, Bo X, Li X, Xu H (2016a) Continuous cavitation designed for enhancing radiofrequency ablation via a special radiofrequency solidoid vaporization process. ACS Nano 10:2549–2558

Zhang K, Li P, He Y, Bo X, Li X, Li D, Chen H, Xu H (2016b) Synergistic retention strategy of RGD active targeting and radiofrequency-enhanced permeability for intensified RF and chemotherapy synergistic tumor treatment. Biomaterials 99:34–46

Publisher's Note Springer Nature remains neutral with regard to jurisdictional claims in published maps and institutional affiliations.